# One-Level Modeling for Diagnosing Surface Winds over Complex Terrain. Part II: Applicability to Short-Range Forecasting

P. ALPERT, B. GETENIO AND R. ZAK-ROSENTHAL

*Department of Geophysics and Planetary Sciences, Tel Aviv University, Israel*

(Manuscript received 6 February 1987, in final form 29 March 1988)

## ABSTRACT

The modified one-level sigma-surface model used by Alpert and Getenio (1988) to study the surface-averaged summertime flow in Israel is run once with the best available information, without tweaking any parameters, for four events consisting of two winter cases (a Cyprus low and a Siberian high), and two summer cases. In a statistical verification for a total of 436 observations, the average direction error, $\overline{\Delta\theta}$, and speed error, $\overline{\Delta V}$, were only $-2.8$ deg and $0.11$ m s$^{-1}$, respectively. However, the averaged absolute direction error, i.e., average $|\Delta\theta|$, was found to be 49.5 deg. Also, the averaged absolute normalized wind speed error, i.e., average $|\Delta V|/V_0$ was found to be 37% for all wind intensities exceeding 4 m s$^{-1}$. Hence, the model's overall wind forecasts were accurate, but not very precise. Although the statistics contain one case, the Siberian high, which was not well simulated, the results (particularly the wind directions) were found to be good. Characteristics of the model are studied through an analysis of variances. Model results were compared to three other models that diagnosed surface wind vectors over complex terrain.

Results suggest that the model is not only capable of diagnosing many details of surface mesoscale flow, but might also be useful for various applications which require operative short-range prediction of the diurnal changes of high-resolution surface flow over complex terrain. Examples of such applications are locating wildland fires, dispersion of air pollutants and prediction of changes in wind energy or of surface wind for low-level air flights.

## 1. Introduction

In Alpert and Getenio (1988; hereafter referred to as AG), the surface winds from a one-level model simulation over complex terrain were compared with observations and three-dimensional modeling results. The one-level model is basically Mass and Dempsey's (1985; hereafter referred to as MD) version, which is a modification of the original model equations proposed by Danard (1977). The simulations were performed for the averaged July surface flow in Israel over a full diurnal cycle. The purpose of AG was to investigate how well a highly simplified, one-level mesoscale model could diagnose detailed surface wind patterns, and how well the model compared with more dynamically complete, three-dimensional models with lower resolution.

The reason for the choice of average summer flow in the Israel region for the validation of the one-level model was threefold. First, the area is known for its high mesoscale activity[1] during summer over complex

terrain. Second, a relatively dense network of surface observations was available with an average spacing of as little as 12 km in the coastal plain of Israel (an area of $\sim$4000 km$^2$). Third, an unusually large number of mesoscale simulations, both two-dimensional and three-dimensional (2-D and 3-D) have been performed in the same region, including the 2-D simulations by Neumann and Mahrer (1971), Doron and Neumann (1977), and Alpert et al. (1982, 1985); and 3-D simulations by Anthes and Warner (1978) and Segal et al. (1982, 1983, 1985). Alpert and Getenio discovered some observed flow patterns that the high-resolution one-level model simulates well, but the lower-resolution 3-D models do not. They also discovered that the one-level model failed to advance the Mediterranean sea breeze (SB) past the central mountain crest in Israel, a severe drawback. This failure is very similar to that reported by Anthes et al. (1980), who attempted to simulate the SB penetration inland with a mixed-layer model. Anthes et al. (1982) used a modified mixed-layer model to show the sensitivity of the SB frontal advance to the treatment of the upper layer. However, the SB was still considerably delayed even in the improved version of their mixed-layer model. Based upon their results and ours, we have suggested that it is unlikely that the correct SB penetration could be simulated by *any* one-level or one-layer model. In particular, the surge of the SB into the Jordan Valley and Lake Kinneret in Israel was shown by Alpert et al. (1982)

---

[1] High mesoscale activity was defined by Alpert and Eppel (1985) as large normalized diurnal wind variability when compared to the interdiurnal one.

---

*Corresponding author address:* Dr. Pinhas Alpert, Dept. of Geophysics and Planetary Sciences, Tel-Aviv University, Tel-Aviv 69978, Israel.

to follow a reversal in the *upper-layer* pressure-gradient force which is difficult, if not impossible, to correctly parameterize in a one-level or one-layer model.

The purpose of this paper is to examine the applicability of the one-level model to real-data forecasting. Keyser and Anthes (1977) performed a similar study with a mixed-layer model, evaluating surface pressure, winds, and potential temperature in the mixed-layer model. We concentrate on surface winds only, providing verification statistics calculated from 43 stations for four case studies. The simulations were performed on an operational basis, although the model was actually run several days after each event. Two of the case studies were chosen to represent typical winter events with low mesoscale activity. The other two were summer cases with high mesoscale activity. We believe that the performance of the model on an *operational* basis represents a stringent test. Danard and Thompson (1983) have illustrated that Danard's (1977) version of the one-level model is capable of diagnosing surface winds, but they applied the model to much smoother terrain (i.e., mainly water bodies) and with a lower resolution.

Sections 2 and 3 describe some aspects of the one-level model: our approach, the four synoptic events, and the subsequent model simulations. Verification statistics and discussion follow in section 4. In the last section, the conclusions regarding the one-level modeling (AG) and its applicability to real-data forecasting are summarized.

## 2. The model—some aspects

The one-level model used in this study is a modification of the Mass and Dempsey (1985) version. The modifications are described in AG. Alpert et al. (1985) and AG presented preliminary results of surface mesoscale flow simulations for average conditions in summer. Here the model is applied to a variety of synoptic situations and some aspects of the diabatic heating and the large-scale input are listed below.

### a. Large-scale input

The temperature and the geopotential heights at 850 mb were interpolated from the nearby five to seven radiosondes and pilot balloons to the model grid through the Cressman analysis (Cressman 1959). The optimum radius of influence $R$ was determined according to Goodin et al. (1979) as

$$R = 1.6\sqrt{A}/N,$$

where $A$ is the domain area and $N$ the number of stations in that domain.

We have adopted 850 mb as the reference level rather than 700 mb, because results were found (in preliminary nonoperational tests) to be more realistic with the 850 mb input. Geopotential data $(Z_R)$ at the reference level were not always sufficient (see Table 1), in which

case the model was allowed to use wind data, and the geopotential height was then calculated from the geostrophic approximation. The following radiosonde and pilot stations were in use: station number 40179 (Bet-Dagan, Israel), 40199 (Eilat, Israel), 40080 (Damascus, Syria), 40265 (Mafraq, Jordan), 40375 (Tabouk, Arabia), 62378 (Cairo, Egypt), and 17607 (Cyprus). The large-scale data, as well as other input parameters in the model, are presented in Table 1.

### b. Diabatic heating

As described in AG, the diabatic heating represents the sensible heat flux convergence term in the thermodynamic equation, $Q/(A_1C_p)$, [see Eq. (2) in AG]. The model is first integrated to a steady state without diabatic forcing. The resulting fields are considered applicable to a "diurnally neutral" time (generally near sunrise or sunset[2]) and the model is then run to the verification time with a specified diabatic forcing. The specification of the forcing follows MD (Fig. 2, p. 1215) where a sine function is applied from presunrise to postsunset with a maximum amplitude $(AH)$, while at night a constant cooling $(AC)$ is prescribed. The heating and cooling amplitudes are estimated from observed surface temperature variations in Israel and are shown in Table 1. The values are, in general, higher—more than double in summer—than those used by MD for their simulation in the state of Washington. At night, a constant value of $0.5°C\ h^{-1}$ was adopted. The corresponding values over water were assumed constant at $0.17$ and $-0.08°C\ h^{-1}$ (corresponding to $1°C/6\ h$ and $1°C/12\ h$, respectively). Sunrise and sunset hours for the four cases to be considered are listed in Table 1.

## 3. Model simulations

The simulations presented in this paper are for Israel and its surroundings in the eastern Mediterranean. The complex topographic features of this region are described in AG (Fig. 1a). This area includes the Mediterranean coastal plain and mountain ranges which reach elevations of 800 to 1000 m and are parallel to the Mediterranean coast approximately 10–30 km inland. Ten to 20 km further east, elevations drop to approximately 400 m below the mean sea level, in the Jordan Rift Valley and the Dead Sea. Somewhat further to the east (another 10–20 km) there is a second mountain range extending from the Golan Heights in the north, to mountains in Jordan which exceed elevations of 1500 m.

Four typical synoptic situations in the eastern Mediterranean were chosen during 1985 in the following order:

---

[2] This is, however, not the case in the present study where simulations with the diabatic heating started at 0000 and 1200 UTC when the synoptic data were available (see discussion later).

TABLE 1. Input data for the model simulations.

a. *The 850 mb data in the following order: $Z_R(m)$, $T_R(K)$ and V (deg/ms⁻¹).*

| RS–SN[a] | Case I. 30 Jan. 0000 UTC | Case I. 30 Jan. 1200 UTC | Case II. 4 Mar. 0000 UTC | Case II. 4 Mar. 1200 UTC | Case III. 30 Jun. 0000 UTC | Case III. 30 Jun. 1200 UTC | Case IV. 11 Jul. 0000 UTC | Case IV. 11 Jul. 1200 UTC |
|---|---|---|---|---|---|---|---|---|
| 40179 | 1468 | — | 1527 | 1520 | 1487 | 1503 | — | — |
|  | 280 | 276 | 275 | 277 | 290 | 293 | 292 | 292 |
|  | — | 220/10 | — | — | — | — | 360/10 | 360/10 |
| 40199 | 1475 | — | — | — | 1490 | 1500 | — | — |
|  | 281.5 | 278 | — | — | 291.5 | 296 | — | — |
|  | — | 220/10 | — | — | — | — | — | — |
| 40080 | 1456 | — | 1521 | — | 1468 | 1473 | — | — |
|  | 280 | 277 | 272 | — | 293 | 297 | 295 | — |
|  | — | 230/10 | — | — | — | — | 090/5 | — |
| 40265 | 1455 | — | 1522 | 1525 | — | — | — | — |
|  | 281 | 277 | 273 | 275 | — | — | — | 296 |
|  | — | 260/5 | — | — | — | — | — | 330/7.5 |
| 40375 | 1484 | — | 1531 | 1527 | 1489 | 1494 | — | — |
|  | 283 | — | 277 | 281 | 294 | 298 | 298 | 298 |
|  | — | — | — | — | — | — | 360/5 | 180/5 |
| 17607 | — | — | — | 1544 | — | 1501 | — | — |
|  | — | — | — | 273 | — | 293 | 293 | 293 |
|  | — | — | — | — | — | — | 360/5 | 020/5 |
| 40378 | — | — | — | — | — | — | — | — |
|  | — | — | — | — | — | — | 289 | 289 |
|  | — | — | — | — | — | — | 060/5 | 140/7.5 |

b. *Additional data.*

| Parameter | Case I | | Case II | | Case III | | Case IV | |
|---|---|---|---|---|---|---|---|---|
| Free atmospheric stability γ (K km⁻¹) | 7.9 | 8.1 | 4.9 | 6.0 | 4.0 | 5.7 | 2.9 | 2.9 |
| Heating amplitude AH (K h⁻¹) | 1.0 | | 1.5 (0.5)[b] | | 2.0 | | 2.0 | |
| Interpolation radius R (Km) | 400 | 300 | 500 | 600 | 300 | 380 | 600 | 600 |
| Water temperature T (K) | 290 | | 290 | | 300 | | 300 | |
| Sunrise (LST) | 0600 | | 0530 | | 0500 | | 0500 | |
| Sunset (LST) | 1700 | | 1800 | | 1900 | | 1900 | |
| Number of steps to steady-state | 390 | 610 | 410 | 900 | 360 | 800 | 410 | 1260 |

[a] Radiosonde station—Synoptic number.
[b] See section 4b and Table 4.

(i)  30 January—Cyprus low,
(ii)  4 March—Siberian high,
(iii)  30 June—Persian trough (developed),
(iv)  11 July—Persian trough (degenerated).

The synoptic title, in each case, follows the common nomenclature in the eastern Mediterranean for the dominant synoptic system at the surface. Because we expected the model to work better for very short range predictions, particularly under highly variable synoptic conditions (e.g. cases I and II), it was run for 3 and 6 h, twice a day. The runs started at 0000 and 1200 UTC (0200 and 1400 LST), when the large-scale input was available, and ended 6 h later in order to predict the surface flow at 0300, 0600 UTC, and at 1500 and 1800

UTC, respectively. The heating/cooling effects from sunrise/sunset, until the starting of the simulations, were not accounted for in the model simulations. They were assumed to be small because the model quickly adjusts itself when the diabatic term is introduced.

The verification statistics were based upon data from 43 surface stations, though only about two thirds of the observations were available (when averaged over all times). Except at 0300 and 0600 UTC 11 July and at 0300 UTC 30 Jan, where only about 15 reports were available, more than 25–30 stations generally provided observations. The exact number of reports for each case and at each forecast are given in Table 2.

In the following experiments, the equations were solved over a 92 × 40 mesh with grid spacing of $\Delta x$
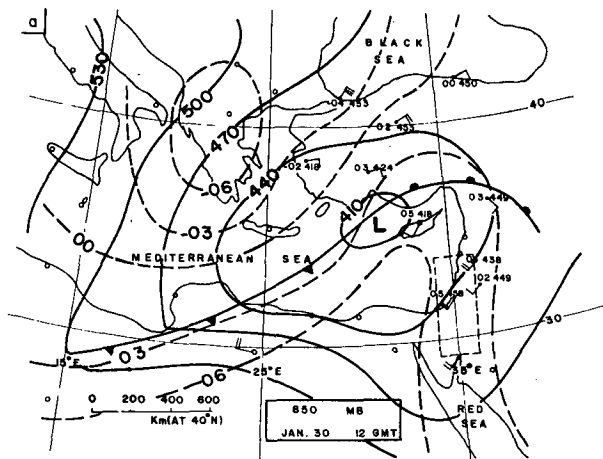
FIG. 1a. Cyprus low: 850 mb chart for 1200 UTC 30 Jan. 1985 in the eastern Mediterranean region based on IMS (Israel Meteorological Service) data. Dashed contours are isotherms with a 3°C interval. Solid contours are isohypses with a 30 m interval. The mesoscale simulated domain is indicated by the dashed rectangle in the southeastern Mediterranean. The observations consist of temperature (degrees Celsius) on the left and geopotential height (meters) on the right of each observational point. As is common, the prefix 1, i.e., 1xxx, for the height was deleted. Each wind barb stands for 10 kt.

$= \Delta y = 5$ km. The time step was 90 sec. The values of the turbulent diffusivities for momentum and temperature were chosen equal, $K_m = K_T = 2 \times 10^4$ m s$^{-1}$. The terrain, drag coefficient ($C_D$), and roughness length ($Z_0$) were defined in AG. All model runs were performed on the CDC 6600 at the computing center of Tel Aviv University.
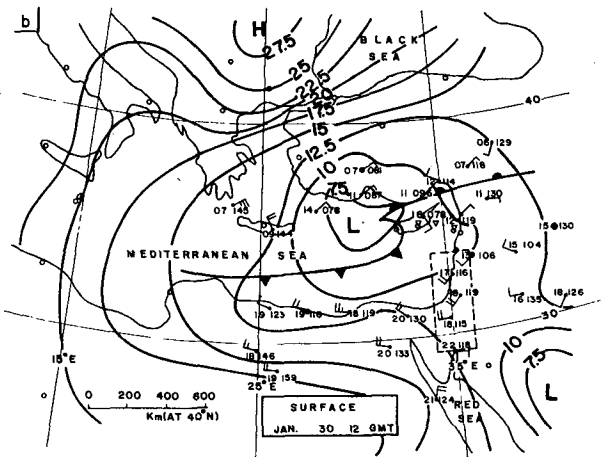


FIG. 1b. Cyprus low: surface chart for 1200 UTC 30 Jan. 1985, in the eastern Mediterranean region based on IMS data. Isobar contours are with a 2.5 mb interval. Observations consist of temperature (degrees Celsius) on the left and pressure in tenths of millibars on the right of the observational point. As common, pressure prefixes 10 and 9, i.e., 10xxx or 9xxx, were deleted. Each wind barb stands for 10 knots.
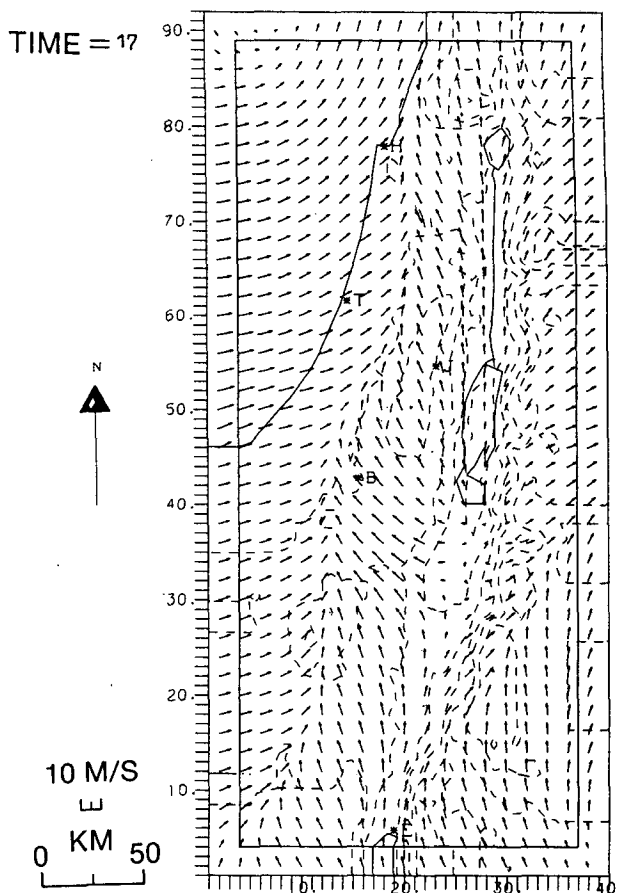


FIG. 1c. Model simulated surface winds for 1500 UTC 30 Jan. 1985. For clearer presentation, only every other vector is indicated. Scales for wind intensity and geographic distance are on the lower left corner. The arrow on the left points to the north. Letters in the figure represent the following locations: H (Haifa), T,(Tel-Aviv), J (Jerusalem), B (Beer-Sheva), and E (Eilat). Time at the upper left is in LST.

The following sections describe the four cases and the eight model runs with the different synoptic patterns, stability and diabatic forcing. Table 1 summarizes some of the model parameters and input data used in this simulations.

*a. Case I: 30 January 1985. A Cyprus low with southwesterly large-scale flow*

Figures 1a–b present the 850 mb and the surface charts at 1200 UTC from 30 January 1985. The cyclonic system shown in these figures is a type common in the region during winter. Local synopticians refer to it as a Cyprus low because its center is frequently located somewhere in the northeastern Mediterranean. The main upper-level trough at 500 mb (not shown here) extends from Turkey to west Egypt. The Cyprus low, in Figs. 1a–b is associated with a secondary trough over the eastern Mediterranean coast. The model domain is indicated in the figures by a dashed rectangle.

TABLE 2. Error statistics classified according to diurnal time and synoptic occasion. Each box contains the averaged results in the following order: $\theta_0$, $\theta_M$ (degrees)—observed and simulated wind directions; $\Delta\theta = (\theta_M - \theta_0)$—direction error; $V_0$, $V_M$ (m s$^{-1}$)—observed and simulated wind speeds; $\Delta V = (V_0 - V_M)$—speed error; and $|\Delta V|/V_0$—absolute normalized error. For scheme of the presentation of the results see box at the bottom left. Values with the sign of #, i.e., $\Delta\theta$ and $\Delta V$, were given only for bottom totals, and not in the rest of the table. The number N at the bottom of each box represents the number of observations in each category. Except in the bottom totals, $|\Delta V|/V_0$ values are only for observed wind speeds which exceed 2 m s$^{-1}$, and these values are followed by the number of the corresponding observations in brackets. The asterisk indicates modified results for case II (see text). Each value in the table contains the standard deviation followed by a ± sign in addition to the average.

| Time (UTC) | 30 Jan | 4 Mar | 30 Jun | 11 Jul | Total |
|---|---|---|---|---|---|
| | 183 ± 71 | 117 ± 64 | 205 ± 70 | 182 ± 108 | 168 ± 83 |
| | 173 ± 36 | 233 ± 74 | 208 ± 40 | 276 ± 66 | 221 ± 65 |
| 0300 | 49 ± 45 | 85 ± 45 | 39 ± 47 | 73 ± 59 | 62 ± 51 |
| | 2.6 ± 1.1 | 3.2 ± 1.7 | 2.8 ± 1.8 | 2.9 ± 1.7 | 2.9 ± 1.6 |
| | 2.0 ± 4.8 | 1.5 ± 8.4 | 3.3 ± 1.1 | 2.2 ± 1.2 | 2.3 ± 1.2 |
| | 0.31 ± .45 (9) | 0.61 ± 0.17 (19) | 0.36 ± 0.31 (18) | 0.38 ± 0.28 (9) | 0.44 ± 0.27 (55) |
| | 15 | 27 | 26 | 13 | 81 |
| | 198 ± 48 | 132 ± 86 | 248 ± 52 | 261 ± 84 | 202 ± 82 |
| | 207 ± 35 | 290 ± 62 | 240 ± 35 | 298 ± 29 | 251 ± 57 |
| 0600 | 35 ± 35 | 102 ± 45 | 37 ± 28 | 45 ± 29 | 55 ± 46 |
| | 3.9 ± 1.6 | 3.1 ± 1.8 | 3.2 ± 1.6 | 3.4 ± 1.5 | 3.4 ± 1.7 |
| | 3.2 ± 0.7 | 2.0 ± 1.2 | 6.0 ± 1.8 | 5.1 ± 1.7 | 3.8 ± 2.1 |
| | 0.28 ± 0.22 (35) | 0.56 ± 0.24 (24) | 0.77 ± 0.58 (24) | 0.60 ± 0.89 (14) | 0.52 ± 0.51 (97) |
| | 39 | 33 | 32 | 16 | 120 |
| | 248 ± 32 | 183 ± 140 | 270 ± 57 | 292 ± 80 | 244 ± 92 |
| | 201 ± 27 | 81 ± 66 | 288 ± 23 | 276 ± 41 | 201 ± 94 |
| 1500 | 52 ± 39 | 48 ± 37 | 27 ± 22 | 43 ± 39 | 44 ± 36 |
| | 4.4 ± 2.1 | 4.1 ± 1.9 | 5.3 ± 2.5 | 5.7 ± 2.4 | 4.8 ± 2.2 |
| | 5.7 ± 6.3 | 5.8 ± 1.4 | 5.9 ± 1.3 | 5.6 ± 1.7 | 5.7 ± 1.3 |
| | 0.54 ± 0.55 (34) | 0.58 ± 0.51 (33) | 0.39 ± 0.27 (25) | 0.38 ± 0.26 (27) | 0.48 ± 0.44 (119) |
| | 37 | 36 | 26 | 28 | 127 |
| | 201 ± 70 | 87 ± 77 | 262 ± 45 | 275 ± 110 | 202 ± 105 |
| | 181 ± 55 | 83 ± 77 | 274 ± 37 | 300 ± 28 | 204 ± 96 |
| 1800 | 60 ± 38 | 31 ± 27 | 33 ± 22 | 37 ± 36 | 41 ± 33 |
| | 3.0 ± 2.0 | 3.8 ± 2.3 | 3.5 ± 2.6 | 3.7 ± 2.0 | 3.5 ± 2.2 |
| | 2.4 ± 3.5 | 3.1 ± 0.8 | 2.8 ± 1.1 | 2.9 ± 0.83 | 2.8 ± 0.8 |
| | 0.32 ± 0.21 (21) | 0.41 ± 0.19 (20) | 0.36 ± 0.22 (18) | 0.32 ± 0.19 (16) | 0.35 ± 0.20 (75) |
| | 30 | 28 | 29 | 21 | 108 |
| $\theta_0$ | 212 ± 58 | 134 ± 104 | 247 ± 61 | 262 ± 100 | 208 ± 96 |
| $\theta_M$ (°) | 195 ± 31 | 170 ± 116 (136 ± 100)* | 252 ± 45 | 287 ± 42 | 219 ± 83 (209 ± 84)* |
| $\Delta\theta$# | −15 ± 60 | 10 ± 81 | −0.9 ± 46 | −7.8 ± 62 | −2.8 ± 65 |
| $|\Delta\theta|$ | 48 ± 39 | 66 ± 48 | 34 ± 31 | 47 ± 42 | 49.5 ± 42 |
| $V_0$ | 3.7 ± 1.9 | 3.6 ± 2.0 | 3.7 ± 2.3 | 4.2 ± 2.3 | 3.73 ± 2.1 |
| $V_M$ (m s$^{-1}$) | 3.6 ± 1.5 | 3.2 ± 2.1 (2.9 ± 2.0)* | 4.5 ± 2.0 | 4.2 ± 2.0 | 3.80 ± 2.0 (3.73 ± 1.97)* |
| $\Delta V$# | −0.05 ± 1.9 | −0.35 ± 2.5 | 0.86 ± 2.6 | −0.02 ± 2.6 | 0.11 ± 2.5 |
| $|\Delta V|/V_0$ | 0.57 ± 0.87 | 0.81 ± 0.91 | 1.35 ± 3.23 | 0.57 ± 0.85 | 0.84 ± 1.83 |
| | N = 121 | N = 124 | N = 113 | N = 78 | N = 436 |

The weather on 30 January 1985 was cloudy and rainy in the northern part of the domain, while in the central region it was partly cloudy with only occasional rain. In the southern part, the weather was nearly clear. Surface southwesterlies of about 10–15 knots blew everywhere in the region (within the dashed rectangle), particularly during the day. Later in the afternoon, the southern region became partly cloudy, but towards nightfall the clouds dissipated, leaving only foggy mountaintops and winds that had weakened appreciably.

The 3-h model-forecast surface winds for 1500 UTC, based upon the 1200 UTC 850 mb large-scale data, are presented in Fig. 1c. The domain in this figure corresponds to the dashed-line rectangle in Figs. 1a–b. The Mediterranean coastal plain is dominated by 5–7 m s$^{-1}$ southwesterlies, which veer to southerly and southeasterlies with similar intensities further inland. There exists a convergence line along the mountain crest which is probably the result of thermal topographic forcing, but the large-scale southerly to southwesterly wind is dominant.

The verification of these results against 43 observations in the region will be presented in section 3b, where the statistical analyses of directions and intensities are discussed.

### b. Case II: 4 March 1985. A Siberian high with easterly cold large-scale flow

In this typical winter situation, the eastern Mediterranean is dominated by the ridge from the semipermanent, massive, cold high-pressure system over the Asian continent. Figures 2a–b present the 850 mb and surface charts for 1200 UTC 4 March 1985. The cold easterlies and northeasterlies are dominant, though light northwesterly SBs were reported on the coastal plain in the afternoon. Small amounts of cirrus clouds were reported in the early morning but they later disappeared and the region became clear. At sunrise, the surface temperatures were close to 0°C in the inland valleys and mountains, but towards noon, temperatures rose to 10°–18°C (see Fig. 2b, which corresponds to 1400 LST).

The simulated surface wind flow for 1500 UTC (Fig. 2c) illustrates the dominance of the easterlies and northeasterlies. Nevertheless, the topographic forcing in the JRV (Jordan Rift Valley) is strong enough to channel the wind to the south, while the general wind direction is toward the southwest. The SBs at the coast have not developed in the model simulation in agreement with the observations, but the SB pressure-gradient force did reduce the intensity of the easterlies at the coast. Venkatesh and Danard (1978) pointed out similar conditions over Lake Ontario.

### c. Case III: 30 June 1985. A Persian trough with northwesterly large-scale flow

The Persian trough at the surface is an extension of the monsoonal low centered northwest of India. It persists through the whole summer with relatively little change. At upper levels, the Azores semipermanent subtropical high dominates the eastern Mediterranean and is associated with a strong subsidence inversion.

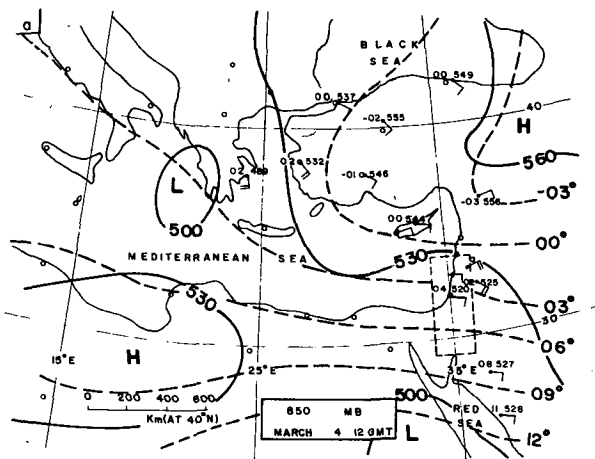In the afternoon, [1400 LST (1200 UTC)], north-

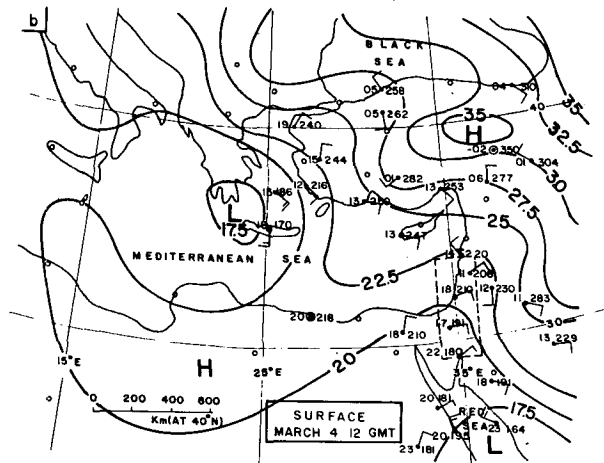FIG. 2b. As in Fig. 1b, but for the Siberian high on 1200 UTC 4 March 1985.

westerlies of 5–10 m s$^{-1}$ blew through the region with nearly clear skies. At this time of the day, the large-scale winds reinforce the local Mediterranean SB to produce relatively strong winds, particularly on the lee
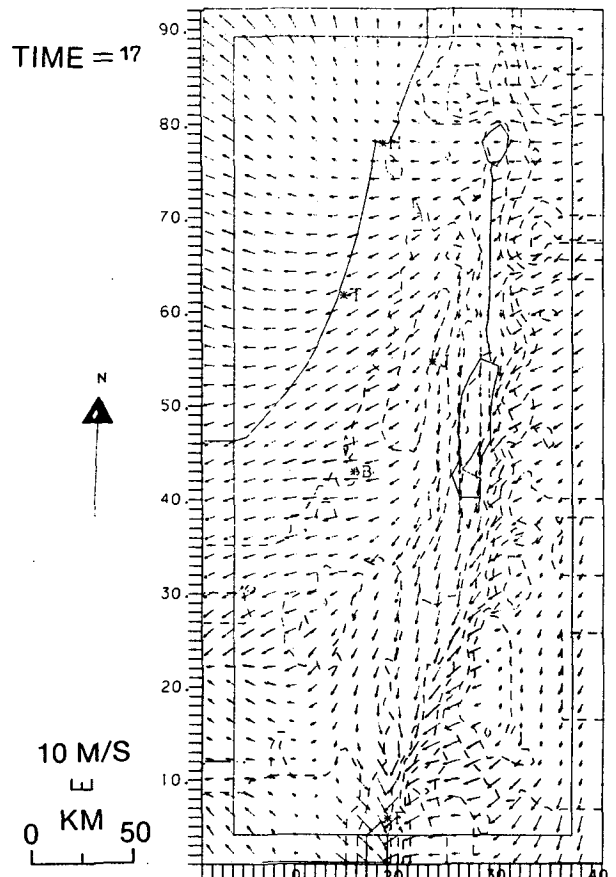
FIG. 2c. As in Fig. 1c model simulated winds, but for 1500 UTC 4 March 1985.

FIG. 2a. As in Fig. 1a, but for the Siberian high on 1200 UTC 4 March 1985.

side of the first mountain range. This was described and discussed in AG for average summer conditions.

The simulated surface wind flow for 1500 UTC (Fig. 3c) illustrates the dominance of the relatively strong northwesterlies. The surface flow circulations are simulated quite well, and even the location of the SB front on the lee side of the mountains is in good agreement with the observations. Unlike the average summer situation discussed in AG, the SB northwesterlies dominate the JRV (northern section). The difference between this case and the simulation of average summer conditions might be explained by the different initial conditions. Here, the simulation started at noon where the large-scale 850 mb flow differs from that adopted in AG to represent averaged summer conditions. This explanation is also supported by the steady-state solution (not shown here) for this case, which does contain northwesterlies in the lee of the mountains.

### d. Case IV: 11 July 1985. A weak Persian trough with north-northwesterly large-scale flow

This is another typical summer synoptic situation, but the monsoonal trough is weaker. One of the criteria used by local forecasters to define the intensity of the Persian trough is the surface pressure difference between Cairo, Egypt and the Gulf of Iskanderun on the Turkish coast. As the Persian trough deepens this difference increases, implying stronger northwesterlies. On 11 July, the pressure difference dropped to 2.2 mb, (see Fig. 4b) as compared to 3.5 mb in case III (see Fig. 3b). As the trough weakens, the Bermuda–Azores subtropical high strengthens in the eastern Mediterranean, the height of the subsidence inversion drops, and the morning and evening stratocumulus clouds become more stratiform and their bases drop. On 11 July, the inversion height was 580 m as compared to 730 m on 30 June. In a recent analysis of the inversion
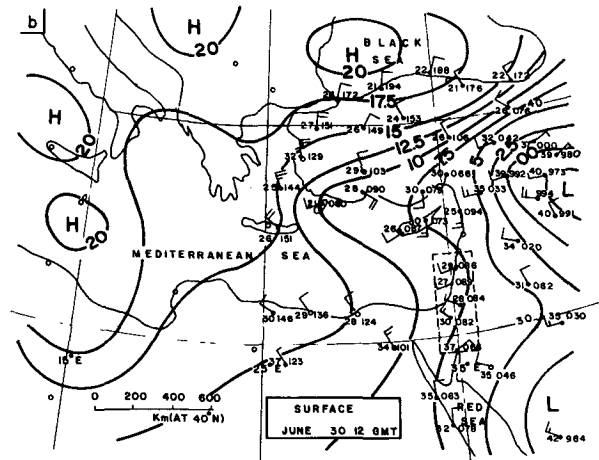


FIG. 3b. As in Fig. 1b, but for Persian trough on 1200 UTC 30 June 1985.

heights for the entire summer (to be published by the authors), the median value was found to be 690 m.

Here, the results of 3-h simulations starting at 0000 UTC are presented. The simulated surface wind flow
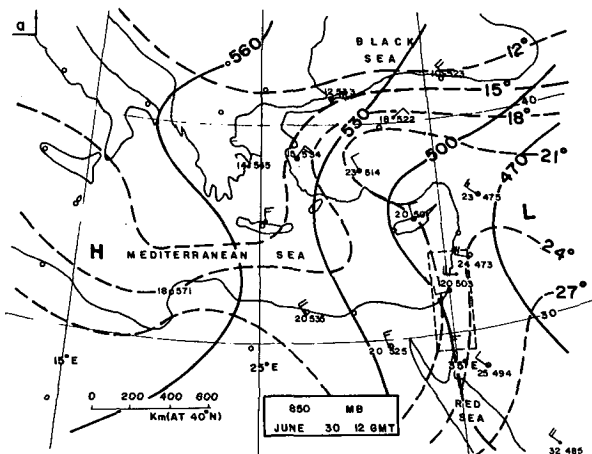


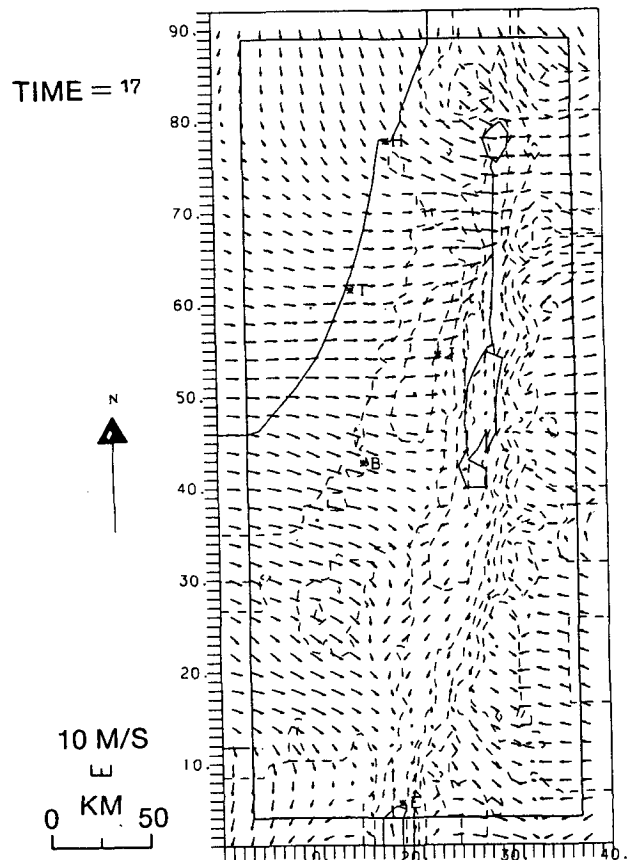FIG. 3a. As in Fig. 1a, but for Persian trough on 1200 UTC 30 June 1985.



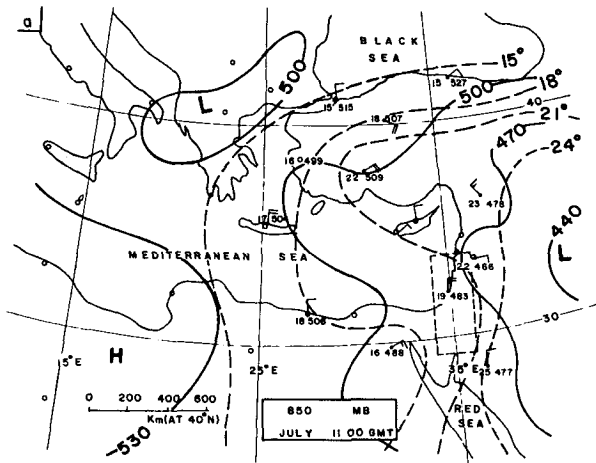FIG. 3c. As in Fig. 1c model simulated winds, but for 1500 UTC 30 June 1985.

FIG. 4a. As in Fig. 1a, but for a weak Persian trough
on 0000 UTC 11 July 1985.

for 0300 UTC (0500 LST) (Fig. 4c), illustrates two
different nocturnal flow features in the early summer
morning. At the coast, southeasterly land breezes sup-
ported by katabatic flow down the mountains prevail,
while over the mountains and on the lee side, the
northwesterlies dominate. The latter are probably the
combination of the large-scale north-northwesterlies
(see Fig. 4a) and the katabatic flow down the lee side
into the JRV.

## 4. Results and discussion

### a. Introduction

In section 3, only 4 of the 16 verification times were
shown. If the observations at all 43 stations were avail-
able, then the verification statistics would have used
$43 \times 16 = 688$ points. But only 436 observations were
reported. For a relatively small subset, as for a specific
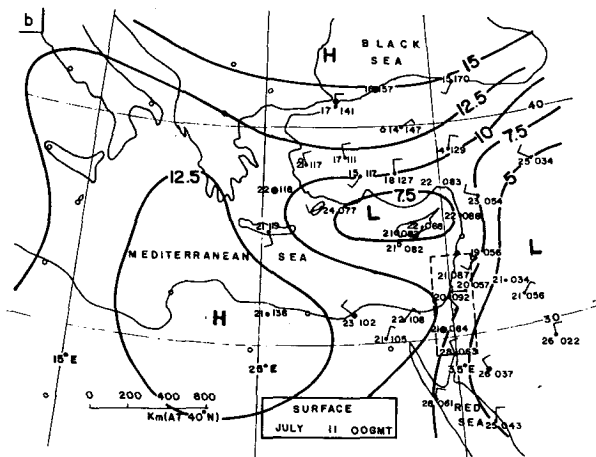


FIG. 4b. As in Fig. 1b, but for a weak Persian trough
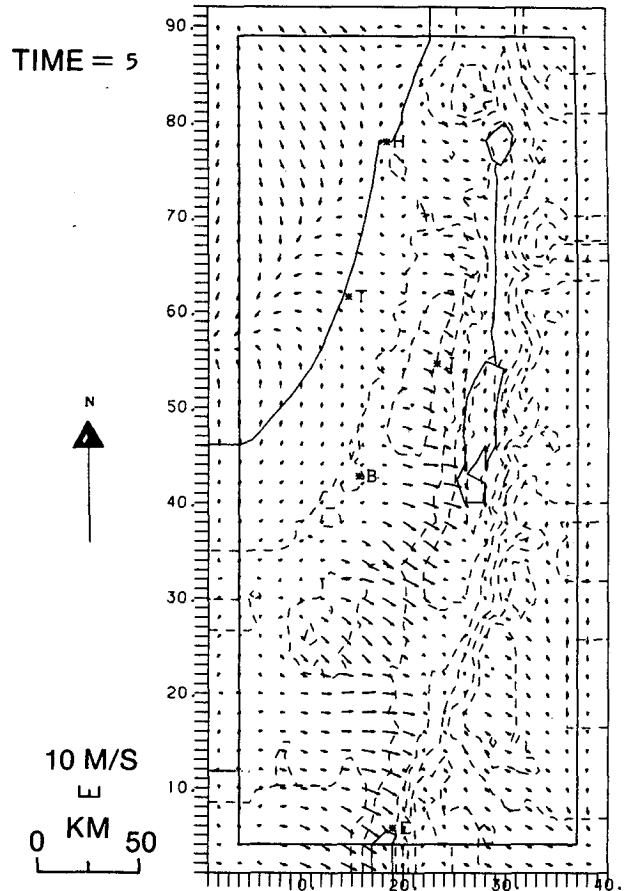on 0000 UTC 11 July 1985.



FIG. 4c. As in Fig. 1c, but for 0300 UTC 11 July 1985.

case and time [order of 25–40 points (see Table 2)],
the results might be highly dependent.

There are many different ways to analyze our results,
depending upon the problem of interest. Wind energy
studies use wind intensities above some critical value,
air pollution studies primarily investigate wind direc-
tions, and groups studying wildland fire danger might
be interested in the diurnal cycle of the wind vector
(see e.g., Ryan 1977). The purpose of this work is to
investigate the applicability of a model to real-data
forecasting; therefore, we have calculated verification
statistics for both wind speed and direction as functions
of time of day and synoptic conditions.

### b. The verification statistics

Table 2 presents the analysis of 436 data points clas-
sified according to the time of day and synoptic situ-
ation. Each box contains the average and standard de-
viation of the following (see scheme in the lower left
box): the observed and simulated wind directions, $\theta_0$
and $\theta_M$; the direction error $\Delta\theta = \theta_0 - \theta_M$ (appears only
for the bottom totals); the absolute direction error
$|\Delta\theta|$; the observed and simulated wind speeds $V_0$ and
$V_M$; the speed error $\Delta V = V_0 - V_M$ appears only for

TABLE 3. The $|\Delta V|/V_0$ statistics for cases I to IV and for the total observations where the lower cutoff of the observed wind speeds varies from 0 to 2, 3, 4 and 5 m s$^{-1}$. Number of observations in each category are given in brackets.

| Min ($V_0$) m s$^{-1}$ | 30 Jan | 4 Mar | 30 Jun | 11 Jul | Total |
|---|---|---|---|---|---|
| 0 | 0.57 ± .87 (121) | 0.81 ± .91 (124) | 1.35 ± 3.23 (113) | 0.57 ± .85 (78) | 0.84 ± 1.83 (436) |
| 2.0 | 0.38 ± .38 (99) | 0.55 ± .35 (96) | 0.48 ± .42 (85) | 0.41 ± .46 (66) | 0.46 ± .40 (346) |
| 3.0 | 0.30 ± .22 (78) | 0.51 ± .29 (75) | 0.42 ± .34 (69) | 0.35 ± .24 (55) | 0.40 ± .29 (277) |
| 4.0 | 0.32 ± .19 (52) | 0.46 ± .24 (51) | 0.35 ± .21 (47) | 0.32 ± .21 (39) | 0.37 ± .22 (189) |
| 5.0 | 0.30 ± .20 (35) | 0.49 ± .23 (31) | 0.35 ± .21 (30) | 0.34 ± .21 (29) | 0.37 ± .22 (125) |

the bottom totals; and the absolute normalized error $|\Delta V|/V_0$, for a sample size $N_V$ for which $V_0 > 2$ m s$^{-1}$. The full sample size is $N$. Values with an asterisk indicate modified results for 4 March 1985, and are discussed in section 5. The following conclusions from Table 2 are straightforward:

1) The observed and simulated average wind speeds for the total sample size of 436 points are very close (see the lower right box).

2) Although the total (in the bottom right) average wind speed error $\Delta V$ is small, 0.11 m s$^{-1}$, the average absolute normalized error $|\Delta V|/V_0$ is large, i.e., 84%. However, this value is misleading because it includes very weak winds for which a relatively small error may result in a very high normalized error. For instance, an error of 1 m s$^{-1}$ for an observed wind of 1 m s$^{-1}$ results in a relative error of 100%. Case III (30 June), which was characterized by weak winds, contributes a very large average normalized error of 135%. In contrast, Table 3 shows average $|\Delta V|/V_0$, calculated only for wind speeds which exceed 2, 3, 4 or 5 m s$^{-1}$. Excluding the weakest winds reduces the absolute average normalized error in the wind speed from 84% to 37%. The reason for eliminating low wind speeds is discussed at the end of this section.

3) The observed and simulated average wind directions are quite close, particularly for 30 June, where $\Delta\theta = -0.9 \pm 46°$, $|\Delta\theta| = 34°$. The absolute wind direction error $|\Delta\theta|$ tends to become smaller in the afternoon hours, particularly during summer.

4) The observed and simulated variances of both directions and speeds are sometimes quite close to each other as, for example, the variances for the total wind speeds for 4 March or total directions for 30 June. Simulated variances, however, are consistently smaller. This is probably due to the fact that the model topography is relatively smooth compared to the real topography. Also, the diffusion terms in the model might be larger than in the atmosphere, and small-scale variations in other types of forcing are not resolved.

5) The worst results are for case II (4 March). In this case, it seems that the SBs in the model were too strong. The model has generated SB westerlies over most of the domain while the observed winds were mostly easterlies, typical for the Siberian high (see results for $\theta_M$ and $\theta_0$ for 0300 and 0600 UTC in

Table 2). When the model was rerun with the daily amplitude of the diabatic heating, $AH$, reduced from 1.5° to 0.5°C h$^{-1}$, the wind direction results improved significantly (see Table 4). Also, when the new results for case II were incorporated into the total verifying statistics, $\theta_M$ changed to 209 ± 84 (from 219 ± 83), compared to the mean observed direction $\theta_0$ of 208 ± 96. The results are marked with an asterisk at the bottom right of Table 2. The mean wind speed dropped, however, from 3.2 to 2.9 m s$^{-1}$, compared to the observed value of 3.6 m s$^{-1}$, but the normalized error has only slightly changed from 0.55 to 0.54.

6) The logarithm of the speed error, $\log(V_0/V_M)$, was found to change consistently in the forecast from 0300 to 0600 UTC in all cases. While it underforecasted $(V_M < V_0)$ at 0300 UTC, the model tended to overforecast $(V_M > V_0)$ at 0600 UTC. In other words, the model increased the wind speed in the morning faster than was observed. Compare also the $V_0$ and $V_M$ values in Table 2. In the evening, a similar but opposite tendency was found from the 1500 to the 1800 UTC forecast. This suggests that the model was overreacting to the changes from day to night, or night to day, possibly due to the abrupt change of the PBL depth by the correction factor in the friction term. Alternatively, this could be the result of a sharp transition in the diabatic heating/cooling when going from night to day, or day to night.

7) From the analysis of wind direction error, in the morning, a consistent decrease of the average errors, $\Delta\theta$, was noticed between 0300 and 0600 UTC for all cases. The model winds turned consistently clockwise

TABLE 4. Statistics for case II in two simulations where the amplitude of the diabatic heating (AH) varies from 1.5 to 0.5 °C h$^{-1}$.

| Parameter | Amplitude of diabatic heating AH (°C h$^{-1}$) | |
|---|---|---|
| | 1.5 | 0.5 |
| $\theta_0$ (°) | 134 ± 104 | 134 ± 104 |
| $\theta_M$ (°) | 170 ± 116 | 136 ± 100 |
| $|\Delta\theta|$ (°) | 66 ± 48 | 60 ± 50 |
| $V_0$ (m s$^{-1}$) | 3.6 ± 2.0 | 3.6 ± 2.0 |
| $V_M$ (m s$^{-1}$) | 3.2 ± 2.1 | 2.9 ± 2.0 |
| $|\Delta V|/V_0$ | 0.55 ± 0.35 | 0.54 ± 0.31 |

more than in the observations. This effect is small but statistically significant (see section 4c and Table 2). In the evening, no consistent tendency was found.

8) In $t$-test analyses for speed errors for each of the 43 stations over all cases, three stations were found to have average speed errors larger than 2.2 m s$^{-1}$. The null hypothesis was that the difference of 2.2 m s$^{-1}$ between the mean speed calculated in the model and the observed wind speed is not statistically significant. This hypothesis was rejected with a 1% level of significance. Examining the results, it was found that one of the stations was located on a mountain peak with strong observed wind speeds ($\sim 10$ m s$^{-1}$), which the model was not able to predict. One possible reason for this is the unrealistic representation of the local topography with 5 km grid spacing, but it could also be due to a nonhydrostatic effect or the unpredicted behavior of the planetary boundary layer at a mountain crest. A second station was located on the Mediterranean coast (in Gaza Port), for which the model predicted strong winds. The actual observed speeds, however, were exceptionally low, possibly due to local screening. At the third station, the number of observations was too small (only 4 out of 16) to provide any statistically significant result.

Another way to evaluate the model performance is to calculate the percentage of the measurements in which the error drops below a certain maximum value as a function of that maximum value. Figure 5 contains
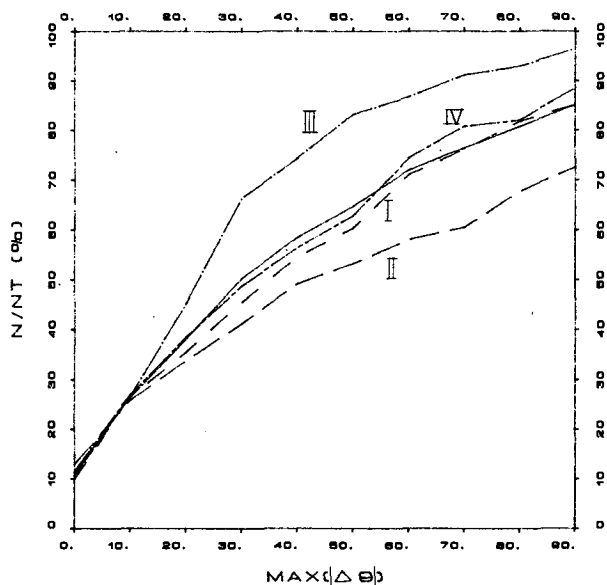


FIG. 5. Percentage of observations, i.e., $N/NT(\%)$, $NT$—total number of observations, for which the absolute direction error, i.e., $|\Delta\theta|$, drops below a certain value between 0 and 90 deg. Results for cases I, II, III, and IV are presented by their respective number and by a different curve as follows: I (dashed), II (dashed with larger segments), III (dashed–dotted) and IV (mixed dashed). Solid curve is for the total.

four such curves for the absolute wind direction error [for cases I, II, III and IV plus the (solid curve) total]. The wind directions on 30 June (case III) are predicted much better than on 4 March (case II). For instance, on 30 June, about 67% of the wind direction errors are below 30°, and 88% are below 60°. The March results are much worse—only about 73% of the direction errors fall below 90°. The poor results for 4 March, which experienced nearly freezing temperatures beneath the Siberian high, are not unexpected for two reasons. First, all of the model coefficients and parameterizations were tuned to the average summer results presented in AG. Also, the SBs were probably reduced on this relatively cold day, because the air temperatures were lower than the water temperature for most of the day.

Figure 6a present similar curves for $|\Delta V|/V_0$, the relative speed error. The 30 Jan and 11 July (cases I and IV) wind speeds were simulated best. As mentioned previously, the 4 March wind speed results were the most poorly simulated. The normalized speed error, again, strongly depends upon wind speeds. For weak winds, it increases to high values which may not fairly represent the model capabilities. Hence, Figs. 6b and 6c show the same curves as in Fig. 6a, but only for observed wind speeds which exceed 2 and 5 m s$^{-1}$, respectively.

Figures 6a–c illustrate how the normalized speed errors decrease when the speed cutoff value is increased from 0 to 2 and 5 m s$^{-1}$, respectively. For instance, the wind speed errors of case I, with a normalized error smaller than 0.3, increase from 48% for all winds to about 56% with a cutoff of 5 m s$^{-1}$ (compare Figs 6a and 6c). With the higher cutoff value of 5 m s$^{-1}$, more than 70% of the January error results fall below 0.4. Also, a normalized speed error above 100% was obtained for about 15% of all results (see solid curve in Fig. 6a where $|\Delta V|/V_0 = 1$), but this percentage drops to only 7% and zero, when the cutoff value is increased to 2 and 5 m s$^{-1}$, respectively (compare Figs. 6b and 6c).

There may be several reasons why low-speed winds are poorly predicted. First, anemometers do not record low wind speeds. The cutoff value depends on instrument type, but for synoptic stations it is of the order of 2 m s$^{-1}$. Second, the influence of the anemometer accuracy on the normalized speed error (through the denominator) becomes much more important for the low wind speeds. Third, low wind speeds seem frequently to be the result of subgrid scale processes that are not explicitly resolved by the model. They are, therefore, not expected to be diagnosed by the present model with a grid spacing of 5 km. Of course, this might also reflect the effects of physical processes that are simply not present in the model. However, the latter two reasons may also apply to high wind speeds. The former factors are necessary in order to explain why the low wind speeds rather than the high ones are poorly predicted.
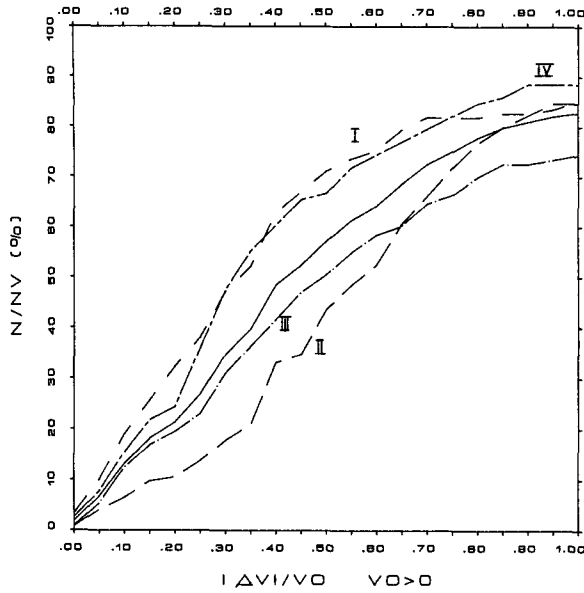
FIG. 6a. Percentage of observations, i.e., $N/NV(\%)$, for which absolute normalized error, i.e., $|\Delta V|/V_0$, drops below a certain fraction between 0 and 1. Different curves for cases I to IV, as in Fig. 5. Solid curve is for all observations.



FIG. 6c. As in Fig. 6a, except only for observed wind speeds which exceed 5 m s$^{-1}$.

## c. Some statistical remarks

(i) Scatter plots (Figures 7a and 7b) present the scatter diagrams for the directions and speeds, respectively. The speed scatter diagram (Fig. 7b) shows that the wind speed error increases with the wind speed. In a logarithmic scatter diagram $\log(V_M/V_0)$—not shown here—the scatter becomes evenly distributed. The di-

rection scatter diagram shows that direction errors appear to be independent of direction. The two groups of points at the lower right and upper left belong to the main scattered domain because of the circular character of direction—see also (iii).

(ii) Histograms. The histograms for the wind direction and speed errors are shown in Figs. 8a and 8b, respectively. These histograms are roughly Gaussian distributions.

(iii) Gaussian distribution for directions. The direction histogram (Fig. 8a) was replotted for the residuals after removing the 16 means. The distribution was found to be reasonably Gaussian and nonskewed, and only approximately five occasions had $|\Delta\theta|$ residuals larger than 150°. Since direction follows a circular base, we examined the number of occasions for which residuals were near 180 deg. This number is small enough ($<5$) that the linear-based treatment (as in Fig. 8a) for the error distribution is valid.

## d. Comparison with other models

The comparison of the performance of different meteorological models is quite difficult when the purposes of the models are not exactly the same. However, if the purpose of all the models considered (i.e., as in this case) is the prediction of surface winds over complex terrain, then one may compare the total performance of each of the models based upon error statistics. However, it should be noted that the models were not necessarily run on the same scale of flow or with the same sort of forcing—see Table 7 for a comparison of the main forcings and horizontal scale in each of the models. Hence, error statistics, as far as they are a function of scale, synoptic-scale forcing or other im-
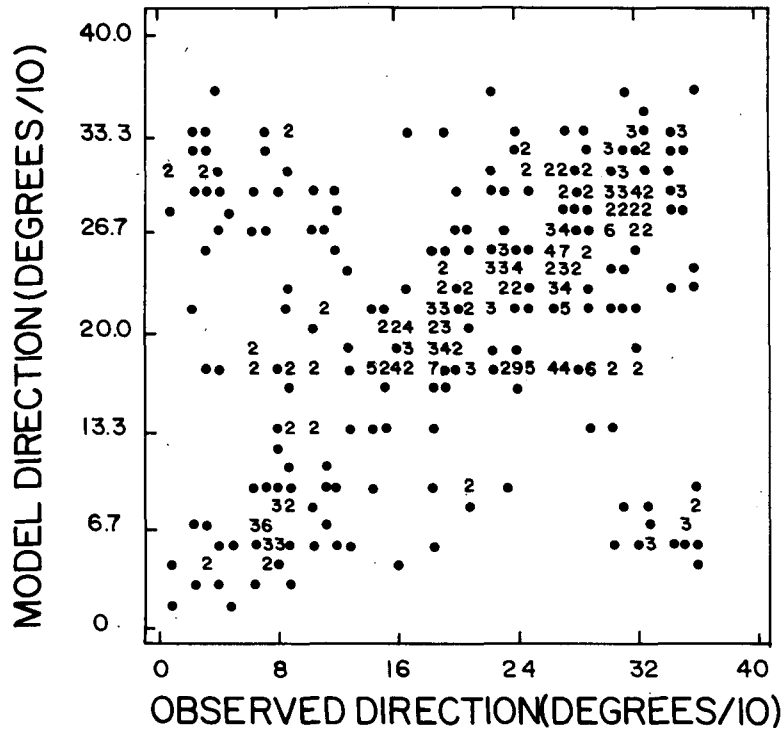


FIG. 6b. As in Fig. 6a, except only for observed wind speeds which exceed 2 m s$^{-1}$.

FIG. 7a. Scatter plot for model compared to observed direction where (●, 2–8) indicate number of occasions and the solid circle stands for 1. The number 9 stands for 9 or greater.
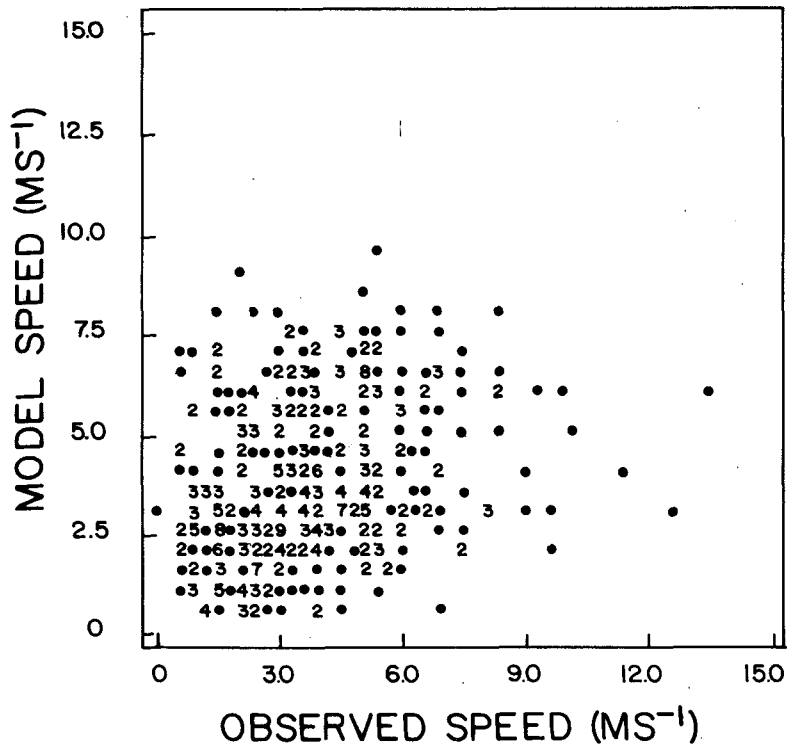


FIG. 7b. As in 7a, except for model versus observed wind speed.

portant aspects of the forcing, have not been considered in the comparison. A full comparison between models could be performed only with the same observed wind fields.

Another potential problem in making a fair comparison is the inclusion in the statistics of the models, those cases for which the models were not necessarily good. Of course, unlike the present model, not all of the models were applied to various synoptic conditions. Hence, comparison with models that deal only with particular synoptic situations may not be fair. The large variability in model performance in different synoptic conditions, as expressed, for instance, in Figs. 5, 6a–c and Table 2, illustrates the difficulty in deriving any conclusion from the comparisons. It still seems valuable, however, to compare different models which have a common purpose, for two reasons. The first is to get

TABLE 5. Statistics of wind speed error $\Delta V$ (m s$^{-1}$) and direction error $\Delta \theta$ (deg) in Danard and Thompson (1983) and in the present study.

| | Danard and Thompson (1983, p. 74, 77) | | Present study synoptic (436) |
|---|---|---|---|
| | Ship + buoys (443) | Seasat (364) | |
| $\Delta V$ (m s$^{-1}$) | $-2.2 \pm 4.2$ | $-3.1 \pm 4.4$ | $0.11 \pm 2.5$ |
| $\Delta \theta$ (°) | $6 \pm 77$ | $10 \pm 37$ | $-2.8 \pm 65$ |

a general measure of what is considered an acceptable or a good result for various applications of surface wind fields. Second, within certain limits such a comparison may help in estimating the capabilities of different models. This could be particularly interesting if the physics and methods of the models are similar.

Table 5 presents the total averaged wind speed error $\Delta V$ and direction error $\Delta \theta$ from Danard and Thompson (1983, p. 74, 77), and from this study. Danard and Thompson compared their model results to winds from ships and buoys and from Seasat, none of which are
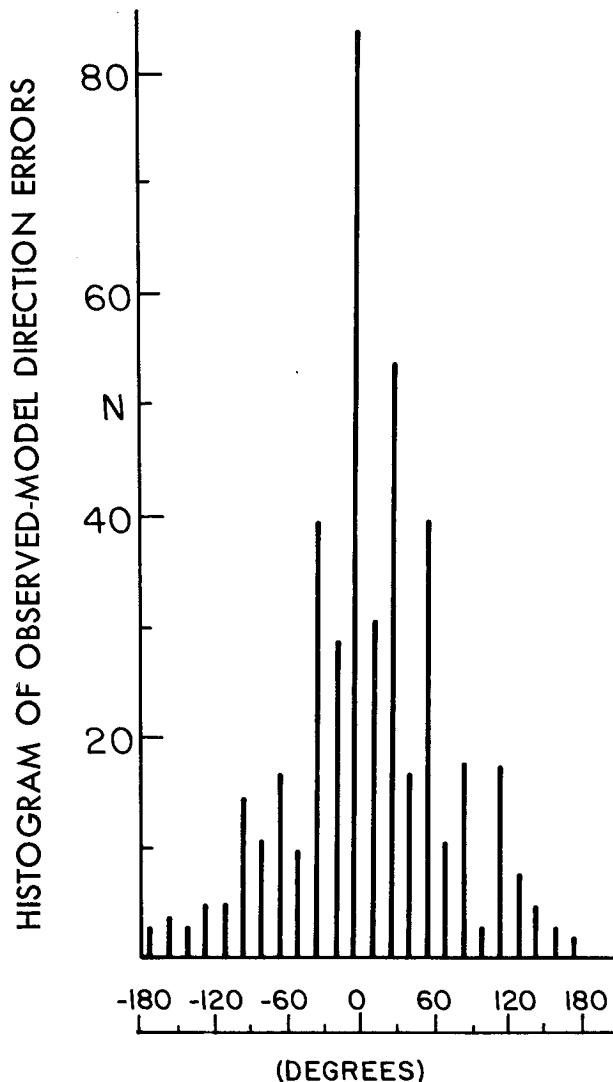
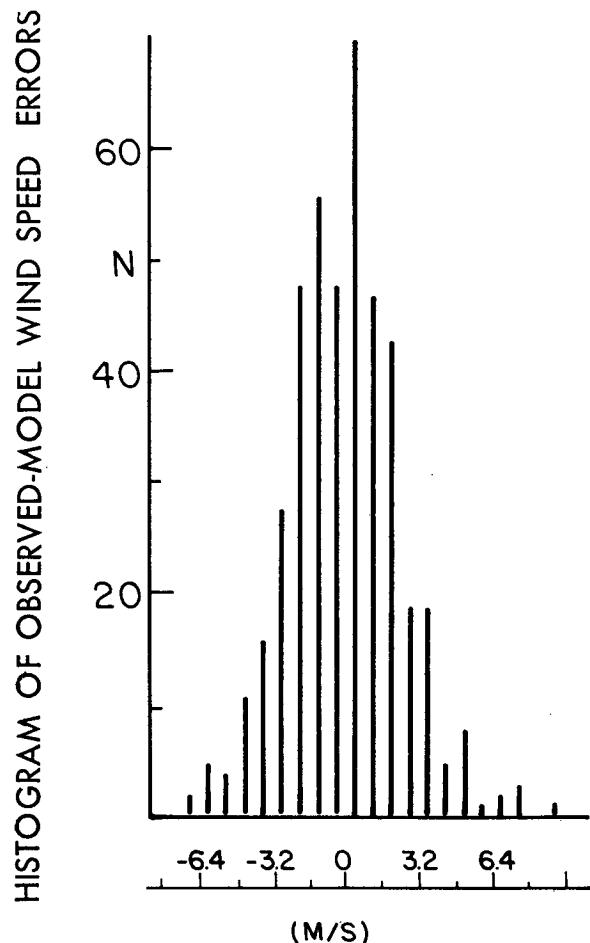FIG. 8a. Histogram of direction errors in intervals of 15 deg.

FIG. 8b. Histogram of speed errors in intervals of 0.8 m s$^{-1}$.

TABLE 6. Statistics of $V_0$, $V_m$, $\theta_0$ and $\theta_m$ and the root mean square errors (RMSEs) for speed (m s$^{-1}$) and direction (deg) from Garret and Smith (1985, p. 178) and in the present study. The $N$ indicates number of observations.

| Investigation | $V_0$ | $V_m$ | RMSE ($V$) | $\theta_0$ | $\theta_m$ | RMSE ($\theta$) | $N$ |
|---|---|---|---|---|---|---|---|
| Garrett and Smith (1985) | 2.72 | 2.86 | 1.18 | 224.2 | 242.9 | 73.6 | 1126 |
| Present study | 3.73 | 3.80 | 1.54 | 208.0 | 219.0 | 42.1 | 436 |

as accurate as synoptic data. In addition, the mean reported speed in the Danard-Thompson experiments was greater—6.1 m s$^{-1}$, compared to 3.7 m s$^{-1}$ in our study—in which case, errors are expected to increase. Comparing the relative skill by $|\Delta V|/V_0$ would be more equitable, but unfortunately $|\Delta V|/V_0$ data from Danard-Thompson were not available. They applied their model to mainly water areas but used a one-level model that is close to our present model.

More recent model results by Garrett and Smith (1985) are presented in Table 6 along with the present model data. The Garret and Smith (1985) model was applied primarily to flow above sloping terrain and was validated using the surface net from the ASCOT project. The RMSE (root-mean-square error) of the wind speed of the present model is 1.54 m s$^{-1}$ compared to 1.18 m s$^{-1}$ in their study, but the RMSE of the wind direction is 42.1°, compared to 73.6° in Garrett and Smith (1985).

A third model for diagnosis and prediction of surface winds is that of Ryan (1977). That analysis follows the diurnal change at only a few stations in the San Bernardino mountains of southern California. The value of the absolute wind direction error at the station CCR for 1 June 1970 (Ryan 1977, p. 580) was found to be $|\Delta\theta| \sim 29.2°$, while the normalized absolute wind speed error $|\Delta V|/V_0$ for wind speeds larger than 2 m s$^{-1}$ is 0.35. When these two values are compared to those in Table 2, the results are very good. However, the results for the additional stations in that study (i.e., MVD and RIM) are worse, particularly for RIM. Some of the characteristics of the model simulations compared here are summarized in Table 7.

## 5. Conclusions

The one-level model performance in four different synoptic situations was investigated and found to perform best when diabatic heating is strong. Statistical verification indicates that the model results compare well with those of other simplified models of different types, which are all aimed at the prediction and diagnosis of surface winds over complex terrain.

It was shown (in AG) that the model is not capable of advancing the Mediterranean SB into the Jordan Rift Valley, a major feature of the mesoscale flow in Israel. However, when the model was initialized with afternoon data in the current study, it succeeded in simulating the northwesterlies in the JRV. This does not imply that the model was able to advance the SB across the mountain crest, because the steady-state solution at 1400 LST simulated the northwesterlies in the JRV. Following this and the verification statistics for the various synoptic events of the present study, we conclude that the model could indeed serve as a useful tool for diagnosing surface winds. This was shown in the present study for relatively short periods of inte-

TABLE 7. Some characteristics of model simulations compared in this study.

| Model reference | Region domain (km) | Latitude (°N) | Dates of observations | Type of model | Topography | Verification data | Main forcing |
|---|---|---|---|---|---|---|---|
| Present study | Israel 450 × 200 | 33 | 4 days in 1985 | One-level constant H | −400 to 1500 m | 43 synoptic stations | Sea-land breeze large-scale topographical |
| Danard and Thompson (1983) | Baffin Bay 450 × 600 | 74 | Aug–Oct 1978 Aug–Sep 1979 | One-level diagnostic H | Mainly water bodies including islands; peaks to 1000–1500 m | Seasat + ship + buoys | Large-scale sea-land breeze topographical |
| Ryan (1977) | San Bernardino Mountains, California 40 × 40 | 34 | 1–2 June 1970 | Semianalytical functions for the various wind vector contribution | 400–1700 m | Four points | Topographical sea-land breeze large-scale |
| Garrett and Smith (1985) | Geysers area– northern California 5 × 5 | 38 | 15 June–15 Sept 1981 | One-dimensional slope flow | 400–900 m | Five points ASCOT project summer averages | Topographical large-scale |

grations, where large-scale changes through the integration have been neglected.

Encouraged by the present results, we currently run the model with an additional prognostic equation for $H$, the depth of the *layer of topographic influence*. Although this has increased the computing time and space requirements—also due to increased numerical instabilities—it is expected to improve the model verification in some cases, thanks to the improved parameterization of the adiabatic inviscid, dynamic interaction between the surface wind and the mass field aloft. An additional prognostic equation for the *planetary boundary layer* depth may also improve the model verification by improving the treatments of friction and diabatic heating/cooling.

## REFERENCES

Alpert, P., A. Cohen, J. Neumann and E. Doron, 1982: A model simulation of the summer circulation from the Eastern Mediterranean past Lake Kinneret in the Jordan Valley. *Mon. Wea. Rev.,* 110, 994–1006.

——, and A. Eppel, 1985: A proposed index for mesoscale activity. *J. Climate Appl. Meteor.,* 24, 472–480.

——, —— and B. Getenio, 1985: Surface wind prediction over complex terrain—Application of a one-level terrain-following model to Israel. *Seventh Conf. on Numerical Weather Prediction,* Montreal, Amer. Meteor. Soc., June 17–20, 369–373.

——, and B. Getenio, 1988: One-level modeling for diagnosing surface winds over complex terrain. Part I: Comparison with three-dimensional modeling in Israel. *Mon. Wea. Rev.,* 116, 2025–2046.

Anthes, R. A., and T. T. Warner, 1978: Development of hydrodynamic models suitable for air pollution and other mesometeorological studies. *Mon. Wea. Rev.,* 106, 1045–1078.

——, N. L. Seaman and T. T. Warner, 1980: Comparison of numerical simulations of the planetary boundary layer by a mixed-layer and multi-level model. *Mon. Wea. Rev.,* 108, 365–376.

——, D. Keyser and J. W. Deardorff, 1982: Further considerations on modeling the sea breeze with a mixed-layer model. *Mon. Wea. Rev.,* 110, 757–765.

Cressman, G. P., 1959: An operative objective analysis scheme. *Mon. Wea. Rev.,* 87, 367–374.

Danard, M., 1977: A simple model for mesoscale effects of topography on surface winds. *Mon. Wea. Rev.,* 105, 572–580.

——, and B. Thompson, 1983: Modelling winds in Lancaster Sound and Northwestern Baffin Bay. *Atmosphere Ocean,* 21, 69–81.

Doron, E., and J. Neumann, 1977: Land and mountain breezes with special attention to Israel's Mediterranean coastal plain. *Israel Meteor. Res. Pap.,* 1, 109–122.

Garret, A. J., and F. G. Smith, 1985: Average diurnal behavior of surface winds during summer at sites in complex terrain. *J. Climate Appl. Meteor.,* 24, 174–183.

Goodin, W. R., G. J. McRae and J. H. Seinfeld, 1979: A comparison of interpolation methods for sparse data: Application to wind and concentration fields. *J. Appl. Meteor.,* 18, 761–771.

Keyser, D., and R. A. Anthes, 1977: The applicability of a mixed-layer model of the planetary boundary layer to real-data forecasting. *Mon. Wea. Rev.,* 105, 1352–1371.

Mass, C. F., and D. P. Demsey, 1985: A one-level mesoscale model for diagnosing surface winds in mountainous and coastal regions. *Mon. Wea. Rev.,* 113, 1211–1227.

Neumann, J., and Y. Mahrer, 1971: A theoretical study of the land and sea breeze circulations. *J. Atmos. Sci.,* 28, 532–542.

Ryan, B. C., 1977: A mathematical model for diagnosis and prediction of surface winds in mountainous terrain. *J. Appl. Meteor.,* 16, 571–584.

Segal, M., Y. Mahrer and R. A. Pielke, 1982a: Numerical study of wind energy characteristics over heterogeneous terrain–central Israel case study. *Bound. Layer Meteor.,* 22, 373–392.

——, Y. Mahrer, and R. A. Pielke, 1983: A study of the meteorological patterns associated with a lake confined by mountains—The Dead Sea case. *Quart. J. Roy. Meteor. Soc.,* 109, 549–564.

——, Y. Mahrer, R. A. Pielke, and R. C. Kessler, 1985: Model evaluation of the summer daytime induced flows over Southern Israel. *Israel J. Earth Sci.,* 34, 39–46.

Venkatesh, S., and M. B. Danard, 1978: A model for computing small-scale wind variations over a water surface. *Bound. Layer Meteor.,* 14, 35–37.